Reaction dynamics of P(^{4}S) + O$_2$(X $^3\Sigma^-$) → O(^{3}P) + PO(X $^2\Pi$) on a global CHIPR potential energy surface of PO$_2$(X ^{2}A$_1$): implication for atmospheric modelling

Guangan Chen[1], Zhi Qin*[1,2], Ximing Li[1], Linhua Liu*[1,2,3]

[1]School of Energy and Power Engineering, Shandong University, 250061, Jinan, China.

[2]Optics and Thermal Radiation Research Center, Institute of Frontier and Interdisciplinary Science, Shandong University, 266237, Qingdao, China

[3]School of Energy Science and Engineering, Harbin Institute of Technology, 150001, Harbin, China

Correspondence to: Zhi Qin (z.qin@sdu.edu.cn) and Linhua Liu (liulinhua@sdu.edu.cn)

Abstract. Reaction dynamics of P(^{4}S) + O$_2$(X $^3\Sigma^-$) → O(^{3}P) + PO(X $^2\Pi$) is thought to be important in atmospheric and interstellar chemistry. Based on the state-of-the-art *ab initio* energy points, we analytically constructed a global potential energy surface (PES) for the ground state PO$_2$(X ^{2}A$_1$) using the combined-hyperbolic-inverse-power-representation (CHIPR) method. A total of 6471 energy points are computed by the multireference configuration interaction method with the Davidson correction and aug-cc-pV5Z basis set. The analytical CHIPR PES reproduces *ab initio* energies accurately with a root-mean-square deviation of 91.5 cm^{-1} (or 0.262 kcal/mol). The strongly-bound valence region of the PES has complicated topographical features with multiple potential wells and barriers. The attributes of the important intermediates are carefully validated with our geometry optimization results and previous computational results. Finally, the reaction probability, integral cross sections and rate constants for P(^{4}S) + O$_2$(X $^3\Sigma^-$) → O(^{3}P) + PO(X $^2\Pi$) are calculated using the quasi-classical trajectory and time-dependent wave packet methods. The trends of probability and integral cross section versus the collision energy can be divided into three stages, which are governed by the entrance barriers or exothermicity of the reaction. The rate constant demonstrates strong Arrhenius linear behavior at relatively low temperatures, but it deviates from this pattern at high temperatures. The calculated cross sections and rate constants are helpful for modelling the P chemistry in atmosphere and interstellar media.

1 Introduction

Phosphorus (P) is one of the essential biogenic elements found in all known organisms. Its compounds are abundant in the biological systems and greatly contribute to the basic biological functions (Maciá, 2005). Much of the P on Earth's surface is locked up in mineral phosphate forms with fairly poor bioavailability, while the P compounds with low oxidation are generally more reactive and accessible for potential prebiotic chemistry (Todd, 2022) but unstable under terrestrial redox conditions (Pasek, 2008).

One source of the P compounds with low oxidation on Earth's surface is interstellar dust particles (IDPs), which account for 99% of the total amount of incoming extra-terrestrial material each year (Plane et al., 2018), containing P with about 8% abundance (Lodders, 2003). The ablation of IDPs in the upper atmosphere of terrestrial planet delivers PO and P (Carrillo-Sánchez et al., 2020), a part of which will undergo a series of chemical processes to form bioavailable H_3PO_3 before reaching the Earth's surface. The corresponding P chemistry networks (Douglas et al., 2019; Douglas et al., 2020; Plane et al., 2021) were predicted by the electronic structure theory, given by

$$P(^4S) + O_2 \rightarrow O + PO \qquad\qquad R1$$

$$PO + O_2 \rightarrow O + PO_2 \qquad\qquad R2$$

$$PO_2 + H(+M) \rightarrow HPO_2 \qquad\qquad R3$$

$$HPO_2 + H_2O(+M) \rightarrow H_3PO_3 \qquad\qquad R4$$

It suggested that the meteor-ablated P is likely oxidized by the reaction R1 first. Hence, the dynamic study for the reaction R1 will contribute to a deeper understanding of the chemical evolution of P and PO in the Earth's atmosphere.

The reaction R1 is also important in astrochemistry. PO has been widely observed in the interstellar medium (ISM) (Tenenbaum et al., 2007; De Beck et al., 2013; Ziurys et al., 2018; Lefloch et al., 2016; Rivilla et al., 2020) and is considered to be the main container for gas-phase P in the ISM (Ziurys et al., 2018; Rivilla et al., 2020). There is some evidence to suggest that PO was present in cometary ices before the birth of the sun (Rivilla et al., 2020) and the comets possibly provided a major source of prebiotic phosphorus compounds (Hernández and Oro, 1997). Hence, the investigation on the formation of PO is helpful for modelling its abundance in ISM.

Given its important role in the interstellar and atmospheric chemistry, the reaction R1 was investigated in several experimental and theoretical works (Douglas et al., 2019; Husain and Norris, 1977; Husain and Slater, 1978; Clyne and Ono, 1982; Henshaw et al., 1987; Gomes et al., 2022). Previous experiments presented its rate constants at a specified temperature about 300 K (Husain and Norris, 1977; Husain and Slater, 1978; Clyne and Ono, 1982; Henshaw et al., 1987) and their values diverged by an order of magnitude. A recent experiment determined the rate constants of P (^4S, ^2D and ^2P) + $O_2 \rightarrow O + PO$ at temperatures ranging from ~200 to 750 K (Douglas et al., 2019). In the same work, the rate constants of $P(^4S) + O_2(X\ ^3\Sigma^-) \rightarrow O(^3P) + PO(X\ ^2\Pi)$ were also computed using the Rice-Ramsperger-Kassel-Markus (RRKM) theory with the molecular geometries optimization at the B3LYP/aug-cc-pVQZ (AVQZ) level. Subsequently, the state-of-the-art *ab initio* method was used to predict the minimum energy path (MEP) of this reaction (Gomes et al., 2022) and the rate constants were computed employing

60   the standard transition state theory (TST). These two theoretical rate constants reproduced the experimental results to some extent and the difference between them came mainly from the predicted barrier heights. The limitation of the former is that the B3LYP method is not good at predicting the barrier heights (Zhao and Truhlar, 2008; Peverati and Truhlar, 2012). Also, the statistical RRKM and TST theories may fail due to unincluded non-statistical dynamic effects (Carpenter, 1998; Thomas et al., 2008), so a dynamic study for this reaction is required. Moreover,

65   their analytical forms of the rate constants were obtained by fitting predictive data lower than 1000 K, so the fitted rate constants at high temperatures may not be accurate. Accurately modelling the rate constants of $P(^4S) + O_2(X\ ^3\Sigma^-) \rightarrow O(^3P) + PO(X\ ^2\Pi)$ in a wide temperature range is desired because of its potential application in the Earth's atmosphere (Carrillo-Sánchez et al., 2020).

        The reactants $P(^4S) + O_2(X\ ^3\Sigma^-)$ and products $O(^3P) + PO(X\ ^2\Pi)$ are connected to the lowest doublet and quartet

70   states of PO_2, in which the doublet state $(X\ ^2A_1)$ plays a major role in this reaction (Gomes et al., 2022). The molecular geometries and vibration frequencies of $PO_2\ (X\ ^2A_1)$ have been well studied by several theoretical (Lohr, 1984; Kabbadj and Liévin, 1989; Jarrett-Sprague and Hillier, 1990; Cai et al., 1996; Francisco, 2002; Xianyi et al., 2008; Liang et al., 2013; Xu et al., 1996; Bauschlicher, 1999) and experimental (Cordes and Witschel, 1965; Davies and Thrush, 1968; Drowart et al., 1972; Verma and McCarthy, 1983; Kawaguchi et al., 1985; Hamilton,

75   1987; Qian et al., 1995; Lei et al., 2001; Lawson et al., 2011) methods. The recent measurement reported $R_{PO} = 2.771\ a_0$ and $\theta_{OPO} = 135.3°$ with the C_{2v} symmetry (Kawaguchi et al., 1985), along with the vibration frequencies of 1075.4 cm⁻¹, 397.3 cm⁻¹ and 1327.54 cm⁻¹ for the symmetrical stretching (ω_1) (Lei et al., 2001), bending (ω_2) (Lei et al., 2001) and antisymmetric stretching (ω_3) (Lawson et al., 2011), respectively. It is worth noting that potential energy surface (PES) can yield physical insight into the reaction path, energy transfer and structure of

80   intermediates. The analytical form of a global PES modeled by *ab initio* energies can accurately predict the barrier height and it is the first step toward molecular simulations, such as the reaction or non-reaction collisions and photodissociation within the system (Conway et al., 2020; Caridade et al., 2013; Schmidt et al., 2013). Therefore, the dynamic study carried out on such a PES is reliable and the information including the reaction probability and integral cross section (ICS) can be well predicted. The first analytical PES of $PO_2\ (X\ ^2A_1)$ was constructed using

85   the B3P86/6-311++G(3df, 3pd) energy points (Zeng and Zhao, 2012), but the dissociation energy was well beyond the experimental value and the intermediates were not all predicted. For carrying out a high-precision dynamic study of the title reaction, it is necessary to develop a global PES of $PO_2\ (X\ ^2A_1)$, in which the potential energies should be calculated at the state-of-the-art *ab initio* method and the reaction path should be well reproduced and carefully validated.

90   This work aims to establish a global PES for the ground state $PO_2(X\ ^2A_1)$, so as to carry out the dynamic study on $P(^4S) + O_2(X\ ^3\Sigma^-) \rightarrow O(^3P) + PO(X\ ^2\Pi)$. The state-of-the-art *ab initio* methods were applied to calculate the potential energies of $PO_2(X\ ^2A_1)$ and the analytical PES was generated using the combined-hyperbolic-inverse-power-representation (CHIPR) method (Varandas, 2013; Rocha and Varandas, 2020, 2021). The rate constants for the $P(^4S) + O_2(X\ ^3\Sigma^-) \rightarrow O(^3P) + PO(X\ ^2\Pi)$ reaction at temperatures ranging from 200 to 5000 K were calculated

95   using the quasi-classical trajectory (QCT) (Peslherbe et al., 1999; Li et al., 2014) and time-dependent wave packet (TDWP) (Zhang and Zhang, 1993, 1994) methods, and were compared with previous experimental and theoretical results. Moreover, the state-specified reaction probability and ICSs were computed in order to get a deeper
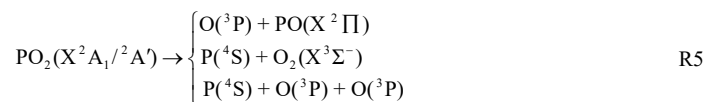
understanding of this reaction.

2 *Ab initio* calculations

100 All *ab initio* calculations of the ground state $PO_2(X\ ^2A_1)$ were carried out using the MOLPRO 2015 software package (Werner et al., 2020; Werner et al., 2015; Eckert et al., 1997) with the $C_s\ (A')$ symmetry point group. The Dunning-type aug-cc-pV5Z (AV5Z) basis set (Dunning et al., 2001; Martin and Uzan, 1998; Woon and Dunning Jr, 1993) was applied. The calculation processes were as follows. Firstly, the Hartree-Fock (HF) method was used to obtain the single-configuration wavefunction of $PO_2(X\ ^2A_1)$. The relevant multi-configuration wavefunctions

105 were generated by the full-valence complete active space self-consistent field (CASSCF) method (Knowles and Werner, 1985) based on the HF wavefunction. Finally, the dynamic correlation energies were considered by the internally contracted multireference configuration-interaction method including the Davidson correction [MRCI(Q)] (Knowles and Werner, 1988; Werner and Knowles, 1988), in which the CASSCF wavefunctions were set as reference. In the CASSCF and MRCI(Q) calculations, 12 active molecular orbitals (9A'+3A") involved 17

110 valence shell electrons and the remaining 14 inner shell electrons were considered in 7 closed core orbitals (6A'+1A"). A total of 6471 ab initio energy points were generated from two grids defined in Jacobi coordinates and six additional grids defined around the important intermediates. In the P-O_2 channel, the grids are defined by $2.0 \le R_{O\text{-}O}/a_0 \le 5.3$, $0 \le r_{P\text{-}OO}/a_0 \le 15.0$, and $0 \le \gamma_{P\text{-}OO}/deg \le 90$. In the O-PO channel, the ranges are defined by $2.4 \le R_{P\text{-}O}/a_0 \le 4$, $2.0 \le r_{O\text{-}PO}/a_0 \le 15.0$, and $0 \le \gamma_{O\text{-}PO}/deg \le 180$. The additional grids around the equilibrium geometry,

115 local minimum and transition states were constructed to be dense enough according to the geometry optimization (OPTG) (Eckert et al., 1997) results obtained from MOLPRO 2015 (Werner et al., 2020; Werner et al., 2015; Eckert et al., 1997).

3 The CHIPR potential energy surface

According to the spin-spatial Wigner-Witmer correlation, the dissociation scheme of the ground state $PO_2(X\ ^2A_1)$

120 can be described by

$$PO_2(X\ ^2A_1/^2A') \rightarrow \begin{cases} O(^3P) + PO(X\ ^2\Pi) \\ P(^4S) + O_2(X\ ^3\Sigma^-) \\ P(^4S) + O(^3P) + O(^3P) \end{cases} \qquad \text{R5}$$

The ground state $PO_2(X\ ^2A_1)$ dissociates adiabatically into $O(^3P) + PO(X\ ^2\Pi)$, $P(^4S) + O_2(X\ ^3\Sigma^-)$ and $P(^4S) + O(^3P) + O(^3P)$. Assuming the energy of infinitely separated $P(^4S) + O(^3P) + O(^3P)$ atoms to be the zero point, the global adiabatic CHIPR PES of the ground state $PO_2(X\ ^2A_1)$ has the following many-body expansion (MBE) (Murrell,

125 1984; Varandas and Murrell, 1977) form:

$$V(\mathbf{R}) = V^{(2)}_{O_2}\left(R_1\right) + V^{(2)}_{PO}\left(R_2\right) + V^{(2)}_{PO}\left(R_3\right) + V^{(3)}_{O_2}\left(\mathbf{R}\right) \qquad (1)$$

where $V^{(2)}$ are the two-body fragments represented by the diatomic potential energy curves (PECs) of $O_2(X\ ^3\Sigma^-)$ and $PO(X\ ^2\Pi)$. $V^{(3)}$ is the three-body fragment. In the CHIPR method (Rocha and Varandas, 2021, 2020; Varandas, 2013), two-body fragments are given by

130

$$V^{(2)}(R) = \frac{Z_A Z_B}{R} \sum_{k=1}^{L} C_k y^k \tag{2}$$

where Z_A and Z_B are the nuclear charges of A and B atoms, respectively. C_k are expansion coefficients of a Lth-order polynomial and y is the basis set consisted of the linear combination of R-dependent functions [see Eq. (4) shown below]. For the AB_2-type species like PO_2, the CHIPR three-body fragment can be simplified to the following permutation symmetric form (Rocha and Varandas, 2021, 2020; Varandas, 2013):

135

$$V^{(3)}(\mathbf{R}) = \sum_{i,j,k=0}^{L} C_{i,j,k} \left[y_1^i \left(y_2^j y_3^k + y_2^k y_3^j \right) \right] \tag{3}$$

where $C_{i,j,k}$ are expansion coefficients for a Lth-order polynomial and y_p are basis sets of coordinates ($p = 1, 2, 3$) for the reference geometry, which are expressed in terms of the Mth-order distributed-origin contracted basis set (Rocha and Varandas, 2021, 2020):

$$y_p = \sum_{\alpha=1}^{M-1} c_\alpha \phi_{p,\alpha} + c_M \phi_{p,M} \tag{4}$$

140   where

$$\phi_{p,\alpha} = \text{sech} \left\{ \gamma_{p,\alpha} \left[R_p - \zeta \left(R_p^{\text{ref}} \right)^{\alpha-1} \right] \right\} \tag{5}$$

and

$$\phi_{p,M} = \left[\frac{\tanh\left(0.2 R_p\right)}{R_p} \right]^6 \text{sech} \left\{ \gamma_{p,M} \left[R_p - \zeta \left(R_p^{\text{ref}} \right)^{M-1} \right] \right\} \tag{6}$$

are primitive bases. $\gamma_{p,\alpha}$ are non-linear parameters and R_p^{ref} represents the origin. The fitting process was carried out
145   in the CHIPR 4.0 program (Rocha and Varandas, 2021). More detailed descriptions for the CHIPR method can refer to the related manuals (Rocha and Varandas, 2021, 2020). In recent years, there has been a lot of global PESs constructed based on this method, such as H_3 (Varandas, 2013), HO_2 (Varandas, 2013), C_3 (Rocha and Varandas, 2019a), C_3H (Rocha and Varandas, 2019b), PH_2 (Chen et al., 2022), NH_2 (Li et al., 2022) and SiC_2 (Rocha et al., 2022).

150   **3.1 Two-body fragment**

Based on Eq (1), the PECs of the ground states $O_2(X\,^3\Sigma^-)$ and $PO(X\,^2\Pi)$ were fitted to the CHIPR form of Eq. (2) to obtain the two-body fragments of the MBE potential of $PO_2(X\,^2A_1)$. *Ab initio* potential energies were calculated at the MRCI(Q) level of theory with the AV5Z basis set. For $O_2(X\,^3\Sigma^-)$, D_{2h} symmetry was chosen with the consideration of 10 active molecular orbitals ($3A_g + 1B_{3u} + 1B_{2u} + 3B_{1u} + 1B_{2g} + 1B_{3g}$) and 2 closed orbitals ($1A_g$
155    $+1B_{1u}$), while 10 active molecular orbitals ($6A_1 + 2B_1 + 2B_2$) and 6 closed orbitals ($4A_1 + 1B_1 + 1B_2$) of C_{2v} symmetry were applied for $PO(X\,^2\Pi)$. A total of 43 and 34 *ab initio* energy points were obtained for $O_2(X\,^3\Sigma^-)$ and $PO(X\,^2\Pi)$, respectively.
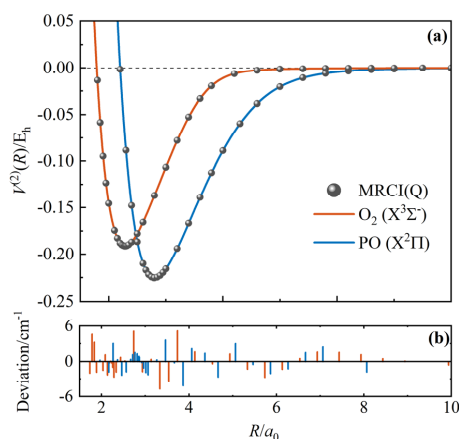
Fig. 1 (a) The PECs of $O_2(X\,^3\Sigma^-)$ and $PO(X\,^2\Pi)$. Solid lines are the CHIPR PECs. Solid circles are *ab initio* energies. (b) The deviations between *ab initio* energy points and the corresponding CHIPR energies.

During the fitting, the 4th-order contracted bases [Eq. (4)] and 8th-order polynomial expression [Eq. (2)] were applied for $O_2(X\,^3\Sigma^-)$ and $PO(X\,^2\Pi)$. Fig. 1 (a) presents the final CHIPR PECs of $O_2(X\,^3\Sigma^-)$ and $PO(X\,^2\Pi)$ with the root-mean-square deviations (RMSDs) of 2.05 cm^{-1} and 1.85 cm^{-1}, respectively. Fig. 1(b) shows the deviations between *ab initio* energy points and the corresponding CHIPR energies, which are within ± 6 cm^{-1}. The obtained CHIPR PECs of $O_2(X\,^3\Sigma^-)$ and $PO(X\,^2\Pi)$ reproduce well with the *ab initio* energy points and exhibit smooth strongly-bound valence region and reasonable dissociation behaviors. As shown in Table 1, the spectroscopic constants of our CHIPR PECs agree well with those of previous theoretical and experimental results. Hence, the CHIPR PECs of $O_2(X\,^3\Sigma^-)$ and $PO(X\,^2\Pi)$ are reliable and can be used as two-body fragments to construct a global the PES of $PO_2(X\,^2A_1)$. The analytic functions of the $O_2(X\,^3\Sigma^-)$ and $PO(X\,^2\Pi)$ PECs are collected in the ready-to-use Fortran code in the Supplement.

Table 1 Spectroscopic constants of the CHIPR PECs of $O_2(X\,^3\Sigma^-)$ and $PO(X\,^2\Pi)$, along with previous theoretical and experimental results.

Method	R_e^a	D_e^b	ω_e^c	$\omega_e\chi_e^c$	α_e^c	B_e^c
$O_2(X\,^3\Sigma^-)$						
CHIPR[d]	2.285	5.203	1583.45	12.05	0.01545	1.4407
Theory[e]	2.281	5.220	1581.16	10.04	0.01254	1.4376
Theory[f]	2.282	5.100	1601			
Exp.[g]	2.282	5.213	1580.19	11.98	0.01593	1.4456
$PO(X\,^2\Pi)$						
CHIPR[d]	2.802	6.130	1227.83	6.65	0.00540	0.7270
Theory[e]	2.787	6.221	1236.01	6.77	0.00574	0.7346
Theory[h]	2.801	6.076				
Exp.[g]	2.789	6.15	1233.34	6.56	0.0055	0.7337

[a] The equilibrium geometry in unit of a_0. [b] The dissociation energy in unit of eV. [c] The units of ω_e, $\omega_e\chi_e$, α_e and B_e are cm^{-1}. [d] The CHIPR PECs. [e] Results at the icMRCI(Q)/CBS(56) + CV + DK level (Liu et al., 2014; Liu et al., 2017). [f] Results at the CCSDT/AVQZ level (Sordo, 2001). [g] Ref. (Huber, 1979). [h] Results at the MRCI(Q)-r/aug-cc-wCV5Z level (Prajapat et al., 2017).

3.2 Three-body fragment

For the CHIPR PES of $PO_2(X\,^2A_1)$, the 4th-order contracted bases [Eq. (4)] and 12th-order polynomial expression
175   [Eq. (3)] were used to fit the three-body fragment. The first trial of the fitted PES presented the complex
topographical features around the reaction path, including the important intermediates of 1 global minimum (GM),
1 local minimum (LM) and 4 transition states (TS). Then, the OPTG was carried out for these configurations and
the additional energy grids were calculated based on the OPTG results. During the subsequent fitting processes,
the weights for the additional grids were set to be 5 and those for the remaining energy points were set to be 1.
180   The final PES was constructed from 6471 *ab initio* energy points, covering an energy range up to 500 kcal/mol
above the GM. Table 2 lists the RMSDs between the analytical CHIPR energies and *ab initio* energies with respect
to the ascending ordered energies and those for the additional energy grids. The GM, LM and TSs of $PO_2(X\,^2A_1)$
were well reproduced by the CHIPR method with RMSDs lower than 25 cm^{-1}. The total RMSD is 91.5 cm^{-1} (or
0.262 kcal/mol), implying the high fitting accuracy and reliability of the CHIPR PES of $PO_2(X\,^2A_1)$. The whole
185    $PO_2(X\,^2A_1)$ PES is collected in the ready-to-use Fortran code in the Supplement.

Table 2 The root-mean-square deviations (RMSDs) with respect to the ascending ordered energies and those for the additional energy grids.

	N	Max deviation	RMSD/cm^{-1}	$N_{>RMSD}$
Energy				
10	1560	95.4	24.6	447
20	1892	103.9	23.1	504
40	1986	152.0	24.4	485
60	2039	185.5	29.4	439
80	2131	226.5	37.9	339
100	2231	263.9	52.9	253
200	5911	280.3	84.4	1218
300	6415	319.1	90.1	1441
500	6471	387.9	91.5	1461
Configuration				
GM	1554	79.7	24.5	452
LM	490	71.4	21.4	140
TS1	810	48.6	20.3	292
TS2	405	29.8	10.5	118
TS3	810	34.1	13.4	242
TS4	810	60.8	14.5	188

4 Features of CHIPR PES

Fig. 2, Fig. 3 and Fig. 4 display the topographical features and the relevant stationary points of the CHIPR PES
190   for the ground state $PO_2(X\,^2A_1)$. Table 3 compares the main attributes of the stationary points for the CHIPR PES
with other theoretical and experimental results, including the interatomic distances for OO (R_1) and PO (R_2 and
R_3), the bond angle (θ) between R_2 and R_3, the vibration frequencies (symmetrical stretching ω_1, bending ω_2 and
antisymmetric stretching ω_3) and the potential energies (E) relative to the $P(^4S) + O(^3P) + O(^3P)$ asymptote. In
particular, our OPTG results for GM, LM, TS1, TS2, TS3 and TS4 are also collected in Table 3, which are

195   calculated at the MRCI(Q) level as implemented in MOLPRO 2015 (Werner et al., 2020; Werner et al., 2015). As shown in Table 3, the attributes of all the stationary points reproduced by CHIPR method are very similar to the OPTG results.
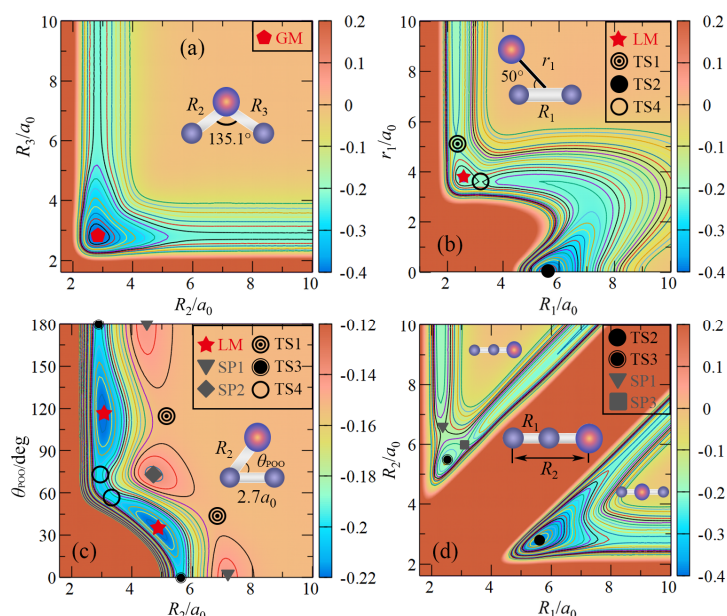
Fig. 2 (a) The contour plot for bond stretching in the OPO bending configuration with θ fixed at 135.1°. Contours are equally spaced by 0.02 E_h, starting from -0.4 E_h. (b) The contour plot for the insertion of the P atom into the O_2 fragment with the insertion angle of 50°. Contours are equally spaced by 0.011 E_h, starting from -0.38 E_h. (c) The contour plot for P moving around one of the O atoms with R_1 fixed at 2.7 a_0. Contours are equally spaced by 0.006 E_h, starting from -0.4 E_h. (d) The contour plot for bond stretching of OOP colinear configuration. Contours are equally spaced by 0.01 E_h, starting from -0.4 E_h.

205   Fig. 2 (a) shows the topographical features of the $PO_2(X\,^2A_1)$ PES for the PO bond stretching from θ fixed at the equilibrium angle of 135.1°. As shown in Fig. 2 (a), the GM of the CHIPR PES has a C_{2v} symmetric configuration with bond lengths of $R_1 = 5.142\,a_0$ and $R_2 = R_3 = 2.788\,a_0$, which can be seen in Fig. 3 (b) and Fig. 4 as well. The vibrational frequencies are computed to be 1137.6 cm^{-1}, 464.7 cm^{-1} and 1460.0 cm^{-1} for ω_1, ω_2 and ω_3, respectively. According to Table 3, these attributes of GM agree well with previous theoretical and experimental results,

210   excepted that ω_3 is slightly higher than experimental results and those calculated by the CCSD(T) method. Fig. 4 (a) presents the barrierless channel of an O atom dissociated from $PO_2(X\,^2A_1)$ and the corresponding dissociation energy D_e(O-PO) of the CHIPR PES is 5.305 eV, which is similar to the experiment value of 5.11 eV (Drowart et al., 1972) and the theoretical result of 5.24 eV at the CCSD(T)/(CBS+SO+DK+CV+ZPE) level (Bauschlicher, 1999). The dissociation energy of the P atom dissociated from $PO_2(X\,^2A_1)$ is predicted to be 6.23 eV, showing a

215   good concordance of the predicted value of 6.15 eV at CI/3-21G* level (Kabbadj and Liévin, 1989).

Fig. 2 (b) and (c) show the entrance channel of $P(^4S) + O_2(X\,^3\Sigma^-) \rightarrow O(^3P) + PO(X\,^2\Pi)$, i.e. the contour plots for the insertion of the P atom into the O_2 fragment with the insertion angle of 50° and for P moving around one of the O atoms with R_1 fixed at 2.7 a_0, respectively. As illustrated in these two figures, the minimum energy path of

the entrance channel is connected by TS1, LM and TS4 in turn, which is in accordance with the earlier prediction

220   (Gomes et al., 2022; Douglas et al., 2019). The most important configuration for the reaction is the entrance barrier of TS1. The barrier height relative to the $P(^4S) + O_2(X\ ^3\Sigma^-)$ asymptote was theoretically predicted to be 0.032 eV at B3LYP/AVQZ level (Douglas et al., 2019) and 0.158, 0.142 and 0.137 eV at MRCI(Q)/AVXdZ (X = T, Q, 5) levels (Gomes et al., 2022), respectively. Our CHIPR PES is fitted by the energies at MRCI(Q)/AV5Z level and the barrier height of TS1 is 0.133 eV, which is particularly consistent with the result at MRCI(Q)/AV5dZ level

225   (Gomes et al., 2022). Also, the attributes of TS1, LM, and TS4 showed good agreement with previous theoretical results, which are presented in details in Table 3.

Table 3 Attributes of the global minimum (GM), local minimum (LM), transition state (TS) and second-order saddle (SP) of $PO_2(X\ ^2A_1)$ CHIPR PES

	Method	R_1/a_0	R_2/a_0	R_3/a_0	θ/deg	ω_1/cm^{-1}	ω_2/cm^{-1}	ω_3/cm^{-1}	E/eV
GM (C_{2v})	CHIPR	5.142	2.788	2.788	134.5	1137.6	464.7	1460.0	-11.435
	AVQdZ[a]	5.118	2.767	2.767	135.3	1085.5	402.1	1495.7	-11.437
	Theory	5.142[b]	2.785[b]	2.785[b]	134.8[b]	1073[b]	390[b]	1349[b]	-11.40[c]
	Theory[d]	5.132	2.775	2.775	135.3	1081.2	391.6	1362.2	
	Theory[e]	5.123	2.786	2.786	133.7	1072.4	389.5	1316.8	
	Theory[f]	5.108	2.785	2.748	134.8	988.4	415.4	1316.4	
	Exp.	5.126[g]	2.771[g]	2.771[g]	135.3[g]	1117[h]	387[h]	1327.5[i]	-11.26[j]
	Exp.					1075.4[k]	397.3[k]	1327.5[l]	
LM (C_s)	CHIPR	2.525	3.074	4.898	26.0	676.0	262.6	1009.9	-6.135
	AV5Z[a]	2.522	3.075	4.857	26.7	709.4	228.9	1029.2	-6.136
	Theory[e]	2.529	3.069	4.912	25.8	671	259	1016	
	Theory[f]	2.548	3.128	4.869	27.6	695.9	276.4	1010.5	
TS1 (C_s)	CHIPR	2.317	4.468	5.858	20.9	1412.4	269.4i	277.1	-5.070
	AV5Z[a]	2.317	4.361	5.827	20.5	1398.6	296.9i	271.9	-5.074
	Theory[e]	2.298	4.766	6.233	18.7	1497	121i	225	
	Theory[f]	2.357	4.121	5.640	21.5	1253.2	426.5i	306.9	
TS2 ($D_{\infty h}$)	CHIPR	5.548	2.774	2.774	180	975.9	434.9i	1360.8	-10.619
	AVTZ[a]	5.610	2.805	2.805	180	1030.4	588.3i	1450.1	-9.786
	AV5Z[a]	5.540	2.770	2.770	180				-10.621
	Theory[m]	5.420	2.710	2.710[r]	180	1199	994i	1707	
	Theory[n]	5.446	2.723	2.723[t]	180				
TS3 ($C_{\infty v}$)	CHIPR	2.475	2.917	5.392	0	1108.6	334.1i	671.8	-5.640
	AV5Z[a]	2.465	2.927	5.392	0				-5.592
TS4 (C_s)	CHIPR	2.922	2.900	4.187	44.2	1071.2	412.9	471.7i	-5.866
	AV5Z[a]	2.898	2.899	4.211	43.4	1051.3	398.6	556.0i	-5.866
	Theory[e]	2.976	2.881	4.038	47.4	1103	392	341i	
	Theory[f]	3.130	2.918	4.797	39.1	956.2	351.9	640.6i	
SP1 ($C_{\infty v}$)	CHIPR	2.356	4.027	6.384	0	401.9i	286.6i	1131.3	-4.520
SP2 (C_{2v})	CHIPR	2.397	4.225	4.225		618.7i	415.2i	1211.0	-4.267
SP3 ($C_{\infty v}$)	CHIPR	3.009	5.849	2.840	0	638.6i	219.4i	1226.8	-5.338

[a] Results from the geometry optimization (OPTG). [b] Results at the CCSD(T)/AVQZ level (Francisco, 2002). [c] Result at the CCSD(T) /(CBS+SO+DK+CV+ZPE) level (Bauschlicher, 1999). [d] Results at the CCSD(T)/AV5Z level (Liang et al., 2013). [e] Results at the B3LYP/AVQZ level (Douglas et al., 2019). [f] Results at the MRCI(Q)/AVTZ+d level (Gomes et al., 2022). [g] Equilibrium geometry deduced from the observed rotational constants (Kawaguchi et al., 1985). [h] The vibrational frequencies from laser induced fluorescence spectrum (Hamilton, 1987). [i] Origin of the v_3 fundamental band obtained from the infrared absorption spectrum (Qian et al., 1995). [j] The experimental atomization energy $D_0(PO_2)$ (Drowart et al., 1972). [k] Vibration frequencies from fluorescence emission and laser fluorescence excitation spectra (Lei et al., 2001). [l] Term value of the v_3 fundamental band obtained from laser absorption spectrum (Lawson et al., 2011). [m] Results at the SCF/3-21G* level (Kabbadj and Liévin, 1989). [n] Results at the SCF/6-31G* level (Lohr, 1984).

Fig. 2 (d) shows the contour plot for bond stretching of R_1 and R_2 at colinear configuration, including the OOP

230   (upper left corner) and OPO (lower right corner) configurations. The notable features here are the OPO colinear

transition state TS2 and POO colinear one TS3. The TS3 is predicted to locate at $R_1 = 2.475\ a_0$ $R_2 = 2.917\ a_0$ and

$R_3 = 5.392\ a_0$, and is connected with two second-order saddle points (SP1 and SP3). The configuration of the

colinear TS2 is $R_2 = R_3 = 2.774\ a_0$ and very close to GM. The potential energy of TS2 is 0.816 eV higher than that

of GM, which is close to previous theoretical results of 1.05 eV and 0.93 eV at the CI/3-21G* level (Kabbadj and

235   Liévin, 1989) and MP3/6-31G* level (Lohr, 1984), respectively. As shown in Table 3, the attributes of TS2 are

similar to those of previous theoretical results (Kabbadj and Liévin, 1989; Lohr, 1984), except that the vibration

frequencies are much less than those obtained at SCF/3-21G* level (Kabbadj and Liévin, 1989).

Fig. 3 (a) is the contour plot for the P atom moving around the center of mass of O$_2$ with R_1 fixed at 2.285 a_0,

which display the smooth long-range behavior of the CHIPR PES. There exist high barriers (SP1 and SP2) on the

240   entrance channel of P(^{4}S) + O$_2$(X $^3\Sigma^-$) when the P atom inserts along the mid-perpendicular or molecular axis of

O$_2$. When the Jacobi approaching angle is about 40 ~ 50°, the P atom is much easier to cross the barrier (TS1) and

reach to LM, followed by the subsequent reaction process. At relative low collision energies, therefore, the

approaching P atom will bond first with one of the two O atoms, rather than with them at the same time. Fig. 3 (b)

shows the contour plot for O moving around the center of mass of PO with R_2 fixed at 2.806 a_0, exhibiting the exit

245   channel of the P(^{4}S) + O$_2$(X $^3\Sigma^-$) → O(^{3}P) + PO(X $^2\Pi$) reaction. As shown in Fig. 3 (b), both TS3 and TS4 can be

evolved from LM, but the dissociation of the system is relatively difficult to occur at TS3 due to the high barrier

SP3 on the dissociation path. The two wells LM and GM represent the POO and OPO isomers, which are separated

by the isomerization barrier TS4. The minimum exit channel is connected by the LM, TS4, GM and TS2 in turn,

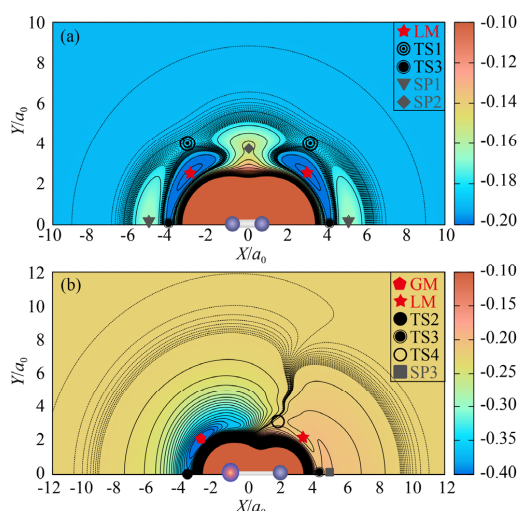and then the system dissociates to the products of O(^{3}P) + PO(X $^2\Pi$).

250

Fig. 3 (a) The contour plot for P moving around the center of mass of O$_2$ with R_1 fixed at 2.285 a_0. Contours are equally spaced by 0.011 E$_h$, starting from -0.22 E$_h$. Dashed areas are contours equally spaced by 0.0005 E$_h$, starting from -0.192 E$_h$. (b) The contour plot for O moving around the center of mass of PO with R_2 fixed at 2.788 a_0. Contours are equally spaced by 0.013 E$_h$, starting from -0.41 E$_h$. Dashed areas are contours equally spaced by 0.0001 E$_h$, starting from -0.226 E$_h$.

255

Fig. 4 depicts the relaxed triangular contour plot (Varandas, 1987) for the CHIPR PES of PO$_2$(X ^{2}A$_1$) using the scaled hyperspherical coordinates ($\beta^*=\beta/Q$ and $\gamma^*=\gamma/Q$), given by

$$\begin{pmatrix} Q \\ \beta \\ \gamma \end{pmatrix} = \begin{pmatrix} 1 & 1 & 1 \\ 0 & \sqrt{3} & -\sqrt{3} \\ 2 & -1 & -1 \end{pmatrix} \begin{pmatrix} R_1^2 \\ R_2^2 \\ R_3^2 \end{pmatrix} \qquad (7)$$

It gives a better view of the major topographical features of the CHIPR PES, including the configurations and
260   symmetries of all stationary points mentioned above. The minimum energy path is connected by TS1, LM, TS4, GM and TS2 in turn. At high collision energies, the P atom is possible to cross the C_{2v} barrier SP2 and reach to GM directly, which will be confirmed in the following dynamic calculations. There is also a collinear abstraction reaction path through TS3, which is difficult to occur due to the mutation of the molecular structure and the existence of collinear barriers (SP1 and SP3) on the entrance and exit channels. We should reiterate that the critical
265   intermediates were carefully verified by the OPTG results, the relevant *ab initio* energy grids were constructed to be dense enough and the CHIPR method reproduced them well. Hence, our CHIPR PES of PO$_2$(X ^{2}A$_1$) has reliable reaction channels and can be used to perform relevant dynamic calculations.
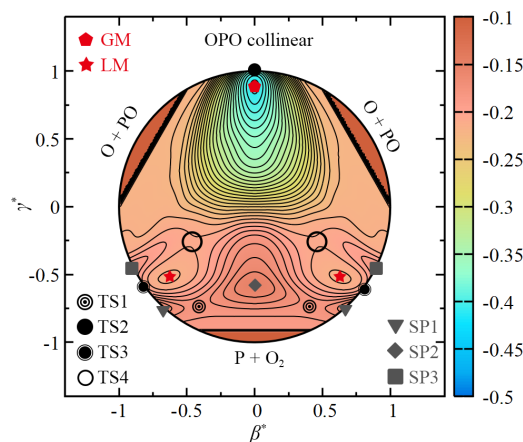

Fig. 4 The relaxed triangular contour plot for the ground-state PO$_2$ in hyperspherical coordinates. Contours are equally
270   **spaced by 0.008 E$_h$, starting from -0.41 E$_h$.**

5 Dynamic calculations

Based on our CHIPR PES of PO$_2$(X ^{2}A$_1$), the reaction probability, ICS and rate constants of the P(^{4}S) + O$_2$(X $^3\Sigma^-$) $\rightarrow$ O(^{3}P) + PO(X $^2\Pi$) reaction were calculated using the QCT and TDWP methods. For each QCT calculations, the sampled trajectories, initial distance of the reactants and integration time step of classical equations of motion
275   were 100000, 15 Å and 0.2 fs, respectively. The state-specified QCT ICS of P(^{4}S) + O$_2$(X $^3\Sigma^-$; v, j) $\rightarrow$ O(^{3}P) + PO(X $^2\Pi$) was calculated by (Li et al., 2014)

$$\sigma_r(E_{tr}; v, j) = \pi b_{max}^2 \frac{N_r}{N} \qquad (8)$$

where b_{max} is the maximum impact parameter, N and N_r represent the total and reactive trajectories, respectively. The state-specified and thermal QCT rate constants $k(T)$ were obtained by (Li et al., 2014)

280

$$k(T) = g_e(T) \left(\frac{8k_B T}{\pi \mu_{P+H_2}} \right)^{1/2} \pi b_{max}^2 \frac{N_r}{N} \tag{9}$$

and

$$k(T) = g_e(T) \left(\frac{2}{k_B T} \right)^{3/2} \left(\frac{1}{\pi} \right)^{1/2} Q_{vj}^{-1}(T) \sum_{vj} (2j+1)$$
$$\times \exp\left(-\frac{E_{vj}}{k_B T} \right) \int_0^\infty E_{tr} \sigma^x \exp\left(-\frac{E_{tr}}{k_B T} \right) dE_{tr} \tag{10}$$

where μ_{P+O_2} is the reduced mass of the reactants, k_B is the Boltzmann constant, $Q_{vj}(T)$ is the ro-vibrational partition function for all the ro-vibrational states of $O_2(X\,^3\Sigma^-)$, E_{vj} is the energy of the (v, j) state and E_{tr} is the translation

285   energy. The rate constant was computed adiabatically for the ground state $PO_2(X\,^2A_1)$ and the electronic degeneracy factor $g_e(T)$ assumed the following form (Graff and Wagner, 1990):

$$g_e(T) = g_{PO_2}(T) \left(q_P(T) q_{O_2}(T) \right)^{-1} \tag{11}$$

where $g_{PO_2}(T) = 2$ is the degeneracy of the ground state $PO_2(X\,^2A_1)$, $q_P(T) = 4$ is the electronic partition function accounting for the fine structure of $P(^4S)$ and $q_{O_2}(T)$ takes into account two spin-orbit states for $O_2(X\,^3\Sigma^-)$, given by

290

$$q_{O_2(^3\Sigma^-)}(T) = g(^3\Sigma_{0^+}^-) + g(^3\Sigma_1^-) \exp(-\Delta / T) \tag{12}$$

where $g(^3\Sigma_{0^+}^-) = 1$, $g(^3\Sigma_1^-) = 2$ due to the doubly degenerate of $\Omega = \pm 1$ and $\Delta = 2.88$ K (2 cm^{-1}) is the spin-orbit splitting between $^3\Sigma_{0^+}^-$ and $^3\Sigma_1^-$ (Liu et al., 2014; Barrow and Yee, 1974).

During the TDWP calculations, the split-operator scheme was used to solve the Schrödinger equation. The Hamiltonian for the reactants (P and O_2) in the PO_2 system can be represented using the Jacobi coordinates:

295

$$H = -\frac{\hbar^2}{2\mu_R} \frac{\partial^2}{\partial R^2} + \frac{(\hat{J} - \hat{j})^2}{2\mu_R R^2} + \frac{\hat{j}^2}{2\mu_r r^2} + V(R, r) + h(r) \tag{13}$$

where R is the distance of the P atom relative to the center-of-mass of O_2, r is the bond distance of O_2, μ_R is the reduced mass between P and O_2, μ_r is the reduced mass of O_2, $\hat{J}$ is the total angular momentum and $\hat{j}$ is the rotational angular momentum of O_2, $V(R, r)$ is the Jacobi form of CHIPR PES for PO_2 and $h(r)$ is the diatomic reference Hamiltonian, given by

300

$$h(r) = -\frac{\hbar^2}{2\mu_r} \frac{\partial^2}{\partial r^2} + V(r) \tag{14}$$

where $V(r)$ is the PEC of O_2.

For the TDWP calculations on the adiabatic PES of $PO_2(X\,^2A_1)$, the time-dependent wave function was expanded by the body-fixed (BF) translational-vibrational-rotational basis:

$$\Psi_{v_0 j_0 K_0}^{JM\varepsilon}(R,r,t) = \sum_{n,v,j,K} F_{nvjK,v_0 j_0 K_0}^{JM\varepsilon}(t) u_n^v(R)\varphi_v(r) Y_{jK}^{JM\varepsilon}(R,r) \tag{15}$$

305 where M and K are the projection of J onto the z axis of the space-fixed and BF coordinates, respectively; $u_n^v(R)$, $\varphi_v(r)$ and $Y_{jK}^{jK\varepsilon}$ are the translational basis, reference vibration eigenfunction for O_2 and total angular momentum eigenfunction, respectively; ε is the parity of the system; n is the label of the translational basis and (v_0, j_0, K_0) denotes the initial ro-vibrational state of O_2.

The dynamic information is extracted from the final wave packet after a long propagation time. The reaction

310 probability $P_{v_0 j_0 K_0}^J(E)$, total reaction cross section $\sigma_{v_0 j_0}(E)$ and temperature-dependent rate constant $k_{v_0 j_0}(T)$ can be calculated by

$$P_{v_0 j_0 K_0}^J(E) = \frac{\hbar}{\mu_r} \text{Im}\left[\psi(E)\left|\delta(r-r_0)\frac{\partial}{\partial r}\right|\psi(E)\right] \tag{16}$$

$$\sigma_{v_0 j_0}(E) = \frac{\pi}{(2j_0+1)k^2}\sum_{K_0}\sum_J (2J+1)P_{v_0 j_0 K_0}^J(E) \tag{17}$$

$$k_{v_0 j_0}(T) = g_e(T)\sqrt{\frac{8k_B T}{\pi\mu_R}}(k_B T)^{-2}\int_0^\infty E\sigma_{v_0 j_0}(E)\exp\left(-\frac{E}{k_B T}\right)dE \tag{18}$$

315 where k is the wavenumber of the initial state with the fixed collision energy E, and k_B is the Boltzmann constant. The parameters used in the TDWP calculations are provided in the Supplement S1.

Fig. 5 presents the CHIPR MEP for $P(^4S) + O_2(X\,^3\Sigma^-) \rightarrow O(^3P) + PO(X\,^2\Pi)$ along with the potential energies of the corresponding intermediates relative to the $P(^4S) + O_2(X\,^3\Sigma^-)$ asymptote. This reaction is an exothermic reaction (-0.927 eV) with an intrinsic entrance barrier TS1 (0.133 eV) and two isomers (LM, GM) separated by the

320 isomerization barrier TS4. Along the MEP, the P atom approaches O_2 at the Jacobi angle of about $40 \sim 50°$ and bonds with one of the two O atoms to form an unstable transition state TS1, followed by a transitory POO isomer LM. The system then evolves through TS4, the OPO isomer GM and the linear transition state TS2, accompanied by the progressively open θ. Finally, the linear PO$_2$ dissociates to the products of $O(^3P) + PO(X\,^2\Pi)$.
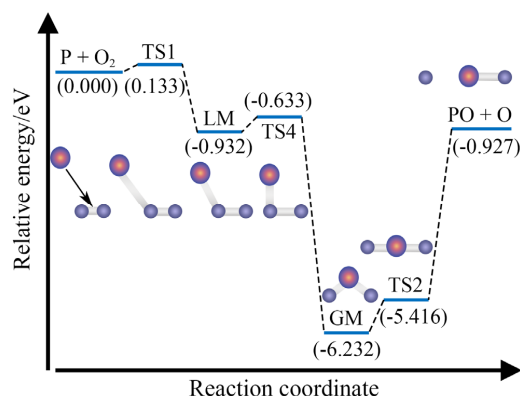

325 **Fig. 5 The minimum energy path and relative intermediates of $P(^4S) + O_2(X\,^3\Sigma^-) \rightarrow O(^3P) + PO(X\,^2\Pi)$. Energies of intermediates relative to the $P(^4S) + O_2(X\,^3\Sigma^-)$ asymptote are given in brackets and in unit of eV.**

The TDWP reaction probability of $P(^4S) + O_2(X\ ^3\Sigma^-;\ v=0,\ j=0) \rightarrow O(^3P) + PO(X\ ^2\Pi)$ at the total angular momentum $J = 0$, 80, 160 and 240 are presented in Fig. 6. For $J = 0$, the probability starts with a threshold and gradually rises to a peak. Subsequently, the probability decreases until the collision energy reaches 0.91eV, then it climbs again
330   and eventually stabilizes. The threshold is about 0.1 eV, resulting from the C_s barrier TS1 (0.133 eV) on the entrance channel. The secondary elevation after 0.91 eV is probably due to the opening of a new entrance channel, i.e. the P atom crosses the C_{2v} barrier SP2 [0.936 eV relative to the $P(^4S) + O_2(X\ ^3\Sigma^-)$ asymptote] along the mid-perpendicular of O_2 and then reaches to GM directly. Both the threshold and the starting point of the secondary elevation are slight smaller than the corresponding entrance barrier heights because of the quantum tunnelling
335   effects. The trend of probability divides into three stages, as marked in Fig. 6. The first and third stages are the two ascending ones in the probability, showing the most common tendency of reactions controlled by barriers (TS1 and SP2). The second stage is the dencending one after the peak, which is dominated by the exothermicity of the reaction. As J increases, the threshold shifts to larger collision energies because of the emergence of the centrifugal barrier.
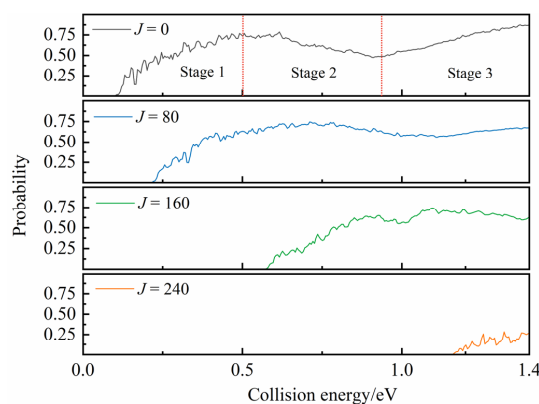

Fig. 6 The TDWP reaction probabilities for $P(^4S) + O_2(X\ ^3\Sigma^-;\ v=0,\ j=0) \rightarrow O(^3P) + PO(X\ ^2\Pi)$ for $J = 0$, 80, 160 and 240 as a function of the collision energy.

The reaction probabilities obtained by the TDWP method are also oscillatory, which is the typical characteristic of quantum resonances. There are numerous bound and quasi-bound states exist in the potential wells LM and GM, so the complexes will be formed there, leading to resonances. Although this reaction is exothermic, the potential
345   energy of the exit channel is still 5.305 eV higher than GM, implying the long-living of the collision complexes and resulting in a plenty of sharp resonances before the peak. As the collision energy increases, the complex becomes short-living, which weakens the quantum resonance and makes the curves of probability smoother.

Fig. 7 displays the state-specified QCT ($v = 0$, 1 and 2) and TDWP ($v = 0$) ICSs for the $P(^4S) + O_2(X\ ^3\Sigma^-;\ v,\ j=0)$
350    $\rightarrow O(^3P) + PO(X\ ^2\Pi)$ reaction as a function of the collision energy. The TDWP ICSs of vibrational excitation were not calculated due to the extremely expensive cost for this reaction involving three heavy atoms and deep potential wells. For $v = 0$ and $j = 0$, both QCT and TDWP ICSs rise rapidly from the threshold (stage 1) and gradually reach a plateau (stage 2), and then increase again and finally stabilized (stage 3). The QCT ICS is less than TDWP ICS and the QCT threshold is consistent with the entrance barrier height but larger than the TDWP threshold, because

355   the QCT method does not include the quantum effects. Meanwhile, the vibrational excitation of O_2 has different effects on the reactivity for the three stages of this reaction. For the stages 1 and 3, the reactivity increases with increasing vibrational excitation, because the increased vibrational energy facilitates the reaction through the path with a barrier, resulting in less collision energy required for high vibrational states. Also, the threshold tends to decrease for the increasing vibrational excitations. For stage 2, where the exothermicity dominates, the vibrational

360   excitations of the reactants suppress the reaction reactivity.
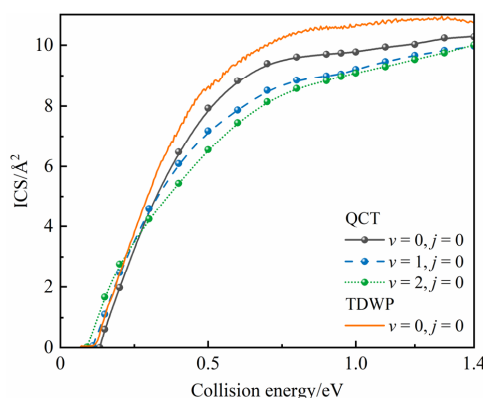
Fig. 7 The state-specified QCT (v = 0, 1 and 2) and TDWP (v = 0) integral cross sections for the P(^{4}S) + O$_2$(X $^3\Sigma^-$; v, j=0) → O(^{3}P) + PO(X $^2\Pi$) reaction as a function of the collision energy.

Fig. 8 presents the state-specified QCT and TDWP rate constants for P(^{4}S) + O$_2$(X $^3\Sigma^-$; v=0, j=0) → O(^{3}P) + PO(X

365      $^2\Pi$) versus the temperature ranging from 200 to 5000 K. This reaction is exothermic and dominated by the entrance barrier TS1, so the rate constants show a significant Arrhenius linear behavior at relatively low temperatures, as shown in Fig. 8 (b). At high temperatures, the rate constants deviate from the Arrhenius behavior, because the effect of the barrier is weakened and the reaction activation energy becomes temperature-dependent. As expected, the TDWP rate constant is higher than QCT rate constant due to the quantum effects, especially at low temperatures.

370   Previous experimental rate constants are also given in Fig. 8 for comparison. Obviously, the rate constants at room temperature determined by various experiments differ by almost an order of magnitude. The earliest two experiments produced extremely large rate constants (Husain and Norris, 1977; Husain and Slater, 1978) and such large values was attributed to the large amounts of secondary dissociation products (Clyne and Ono, 1982). The subsequent experiments were carefully performed to minimize this possible effect and obtained relatively lower

375   rate constants (Clyne and Ono, 1982; Henshaw et al., 1987; Douglas et al., 2019), in which the recent experiment presented the temperature-dependent rate constants (Douglas et al., 2019). As shown in the Arrhenius plot of Fig. 8 (b), however, the recent experimental rate constants do not exhibit a good linear behaviour, unless the values at maximum and minimum temperatures are excluded. Therefore, four experimental rate constants at about 300-600 K are expected to be more reliable. As shown in Fig. 8, the present QCT and TDWP rate constants are lower than

380   the experimental values. It is partly because our rate constants only considered the PES of PO$_2$(X ^{2}A$_1$) corresponding to the P(^{4}S) + O$_2$(X $^3\Sigma^-$) → O(^{3}P) + PO(X $^2\Pi$) reaction, while the experimental rate constant for P(^{4}S) + O$_2$ → O + PO includes other possible process with excited states of O$_2$, O and PO that can be responsible for the depletion of P(^{4}S).

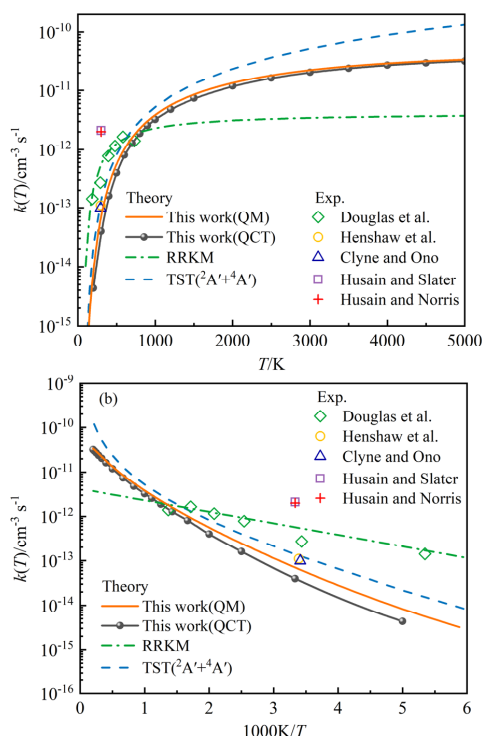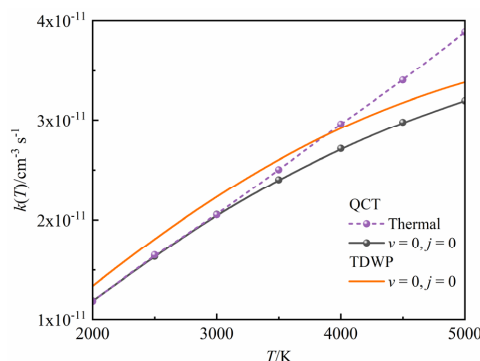**Fig. 8 (a) The state-specified rate constant $k(T)$ for the $P(^4S) + O_2(X\,^3\Sigma^-; v=0, j=0) \rightarrow O(^3P) + PO(X\,^2\Pi)$ reaction as a function of temperature. (b) The corresponding Arrhenius plot. The green chain dotted line corresponds to the theoretical $k(T)$ ($150 \leq T/K \leq 1400$) of $P(^4S) + O_2$ based on the RRKM theory (Douglas et al., 2019). The blue dashed line corresponds to the theoretical rate constant of $P(^4S) + O_2(X\,^3\Sigma^-) \rightarrow O(^3P) + PO(X\,^2\Pi)$ based on the TST and carried out on MEPs of the $^2A'$ and $^4A'$ electronic states of PO$_2$ (Gomes et al., 2022). Diamond represents the experimental value using pulsed laser photolysis-laser-induced fluorescence technique (Douglas et al., 2019); Circle denotes the experimental value using discharge-flow method (Henshaw et al., 1987) ; triangle represents the experimental value using resonance-fluorescence detection in a discharge-flow system (Clyne and Ono, 1982); quadrate denotes the experimental value using resonance fluorescence method (Husain and Slater, 1978); cross represents the experimental value obtained from the attenuation of atomic resonance radiation in the vacuum ultraviolet (Husain and Norris, 1977).**

The theoretical rate constants based on the RRKM[4] theory and TST (Gomes et al., 2022) are also shown in Fig. 8, which are fitted from the calculated data at the temperature below 1000 K. The rate constant obtained by TST includes the contribution of the doublet ($^2A'$) and quartet ($^4A'$) electronic states of PO$_2$ corresponding to $P(^4S) + O_2(X^3\Sigma^-)$, in which the $^4A'$ state works at temperatures above about 600 K (Gomes et al., 2022). At low temperatures, both QCT and TDWP calculations underestimate the rate constant with respect to previous calculations, which can be explained by the fact that the low-temperature reactivity of such barrier-dominated reaction like $P(^4S) + O_2(X\,^3\Sigma^-) \rightarrow O(^3P) + PO(X\,^2\Pi)$ depends sensitively on the entrance barrier height. The entrance barrier height adopted when calculating the RRKM rate constant was obtained to be 0.032 eV at B3LYP/AVQZ level (Douglas et al., 2019). This barrier height was also predicted to be 0.158, 0.142 and 0.137 eV at the MRCI(Q)/AVXdZ (X = T, Q, 5) levels (Gomes et al., 2022), in which the MRCI(Q)/AVTdZ result was modified to be 0.105 eV by including zero-point energy (ZPE) correction, and then used to the TST study (Gomes et al., 2022). There is evidence that the B3LYP method is not good at predicting the barrier heights on the reaction

path (Zhao and Truhlar, 2008; Peverati and Truhlar, 2012). Our CHIPR PES is fitted by the potential energies at MRCI(Q)/AV5Z level and the entrance barrier height is 0.133 eV, which is particularly consistent with the result

410   at MRCI(Q)/AV5dZ level (Gomes et al., 2022), so the CHIPR PES is accurate and reliable. The relatively small QCT rate constants at low temperatures are due to the ZPE problem in the QCT treatment. The TDWP rate constants consider the tunnelling through the entrance channel barrier and the threshold of ICS is about 0.1 eV, agreeing with the modified barrier height (0.105 eV) used in the TST calculation. Whereas, the TDWP rate constants are still slightly lower than the TST rate constants at low temperatures, probably because the TST

415   calculation is carried out only on MEPs, resulting in higher predicted reactivity relative to those of our dynamic calculation considering all possible reaction paths on a global PES.

At high temperatures, previous two theoretical rate constants were predicted by fitting the Arrhenius formula without high-temperature data backing, which could potentially lead to certain errors. The fact that our QCT and TDWP rate constants deviate from the Arrhenius behaviour at high temperatures could confirm this potential

420   problem. As shown in Fig. 8, the rate constants obtained by RRKM theory are obviously lower than our QCT and TDWP rate constants at high temperatures, because the original Arrhenius formula $[4.2 \times 10^{-12} \exp(-600/T)]$ applied for the RRKM rate constants assumes that the reaction activation energy is temperature-independent, which is not applicable at high temperatures. The rate constants obtained by TST $[1.44 \times 10^{-12}(T/300)^{1.66} \exp(-600/T)]$ include the contribution of the $^4A'$ state for PO_2, which are larger than our results. Note that the population of the ro-

425   vibrational excited O_2 increases at high temperatures, which could affect the reaction activity according to the analysis of ICS above. Fig. 9 compares the state-specified ($v = 0, j = 0$) QCT and TDWP rate constants and thermal QCT rate constant for $P(^4S) + O_2(X\ ^3\Sigma^-) \rightarrow O(^3P) + PO(X\ ^2\Pi)$ versus the temperature ranging from 2000 to 5000 K. The thermal TDWP rate constant was not calculated due to the extremely expensive cost. As shown in Fig. 9, the ro-vibratioal ground state ($v = 0, j = 0$) O_2 plays an absolute dominant role at temperatures below 3000 K, while

430   the ro-vibrational excited O_2 appears at temperatures above 3000 K and promotes the reactive activity. Hence, our TDWP rate constant is reliable at temperatures below 3000 K, while it probably underestimates the rate constant at temperatures above 3000 K due to the neglect of the ro-vibrational excitation of O_2. The state-specified ($v = 0, j = 0$) QCT and TDWP rate constants and thermal QCT rate constant are fitted using the three-parameter Arrhenius formula and summarized in the Supplement S2.

435

Fig. 9 The state-specified ($v = 0, j = 0$) QCT and TDWP rate constants and thermal QCT rate constant for the $P(^4S) + O_2(X\ ^3\Sigma^-) \rightarrow O(^3P) + PO(X\ ^2\Pi)$ reaction as a function of temperature.

6 Conclusions

In this work, we have constructed a global CHIPR PES of the ground state $PO_2(X\,{}^2A_1)$ based on a total of 6471 *ab initio* energy points computed at the MRCI(Q)/AV5Z level. The *ab initio* grids for the critical intermediates are constructed to be dense enough based on the OPTG results. The total RMSD of the CHIPR PES is 91.5 cm^{-1} and the RMSDs for the critical intermediates are lower than 25 cm^{-1}. The PES presents complex topographical features with multiple potential wells and barriers. The long-range interactions, diatomic potentials and dissociation energy of each asymptotic channels are reasonable reproduced. The attributes of the main intermediates agree well with available experimental and theoretical results as well as our OPTG results. The corresponding adiabatic MEP of $P({}^4S) + O_2(X\,{}^3\Sigma^-) \rightarrow O({}^3P) + PO(X\,{}^2\Pi)$ features the barrier insertion of the P atom into the O_2 bond at the Jacobi angle of about $40\sim50°$, and the reaction then evolves through LM, TS4, GM and TS2 in turn. Based on the CHIPR PES, the state-specified reaction probability and ICSs for this reaction are calculated using QCT and TDWP methods. The results show three stages of reaction controlled by barrier TS1 (stage 1), exothermicity (stage 2) and barrier SP1 (stage 3) in turn. The vibrational excitation of O_2 promotes the reaction in stages 1 and 3, but suppresses the reactivity in stage 2. Meanwhile, the state-specified and thermal rate constants are predicted for the temperatures ranging from 200 to 5000 K, and then compared with available experimental and theoretical results. The rate constants show a significant Arrhenius linear behavior at relatively low temperatures, but they deviate from the Arrhenius behavior at high temperatures. The ro-vibratioal ground state O_2 plays an absolute dominant role at temperatures below 3000 K, while the ro-vibrational excitation of O_2 promotes the reactive activity at temperatures above 3000 K.

The presented CHIPR PES of $PO_2(X\,{}^2A_1)$ can be used for the molecular simulations of the reaction or non-reaction collisions and photodissociation of PO_2 system in atmospheres and interstellar media. It can also be a reliable component for constructing other larger molecular systems containing PO_2, such as PO_3 and HPO_2 correspond to the reactions R2 and R3 for generating H_3PO_3 in the Earth's atmosphere. The computed reaction probability, ICSs and rate constants may help to explain the relevant thermochemical reactions in related atmospheric and interstellar media.

Data availability. Additional relevant data and supporting information are given in the Supplement. All data used in this study are available upon request from the corresponding authors.

Supplement. The Supplement collects the parameters used in the TDWP calculations and the analytical fitted rate constants. The ready-to-use Fortran code for the whole CHIPR PES of $PO_2(X\,{}^2A_1)$ is also given, including the CHIPR function and all the coefficients of the $O_2(X\,{}^3\Sigma^-)$ and $PO(X\,{}^2\Pi)$ PECs and three-body fragment.

Competing interests. We declare that we have no conflict of interest.

References

475   Barrow, R. F., and Yee, K. K.: The $^3\Sigma^-$ ground states of the group VI-VI molecules, O_2, SO... Te_2, Acta Physica Academiae Scientiarum Hungaricae, 35, 239-246, 1974.

Bauschlicher, C. W.: Heats of Formation for PO_n and PO_nH (n = 1 - 3), The Journal of Physical Chemistry A, 103, 11126-11129, 1999.

Cai, Z., Hirsch, G., and Buenker, R. J.: *Ab initio* study of the electronic spectrum of the PO_2 radical, Chem. Phys.
480   Lett., 255, 350-356, 1996.

Caridade, P., Horta, J., and Varandas, A.: Implications of the O + OH reaction in hydroxyl nightglow modeling, Atmos. Chem. Phys., 13, 1-13, 2013.

Carpenter, B. K.: Dynamic behavior of organic reactive intermediates, Angewandte Chemie International Edition, 37, 3340-3350, 1998.

485   Carrillo-Sánchez, J. D., Bones, D. L., Douglas, K. M., Flynn, G. J., Wirick, S., Fegley Jr, B., Araki, T., Kaulich, B., and Plane, J. M.: Injection of meteoric phosphorus into planetary atmospheres, Planet Space Sci., 187, 104926, 2020.

Chen, G., Qin, Z., Li, J., and Liu, L.: A global CHIPR potential energy surface of PH_2 (X $^2B_1$) via extrapolation to the complete basis set limit and the dynamics of $P(^2D) + H_2(X\ ^1\Sigma_g^+) \rightarrow PH(X\ ^3\Sigma^-) + H(^2S)$, Phys. Chem. Chem.
490   Phys., 24, 19371-19381, 2022.

Clyne, M. A., and Ono, Y.: Kinetic studies of ground-state phosphorus atoms, Journal of the Chemical Society, Faraday Transactions 2: Molecular and Chemical Physics, 78, 1149-1164, 1982.

Conway, E. K., Gordon, I. E., Tennyson, J., Polyansky, O. L., Yurchenko, S. N., and Chance, K.: A semi-empirical potential energy surface and line list for $H_2^{16}O$ extending into the near-ultraviolet, Atmos. Chem. Phys., 20, 10015-
495   10027, 2020.

Cordes, H., and Witschel, W.: Einige Aussagen zur Oxydation des Phosphors, Zeitschrift für Physikalische Chemie, 46, 35-48, 1965.

Davies, P. B., and Thrush, B. A.: The reactions of atomic oxygen with phosphorus and with phosphine, Proceedings of the Royal Society of London. Series A. Mathematical and Physical Sciences, 302, 243-252, 1968.

500   De Beck, E., Kamiński, T., Patel, N. A., Young, K. H., Gottlieb, C. A., Menten, K. M., and Decin, L.: PO and PN in the wind of the oxygen-rich AGB star IK Tauri, Astron. Astrophys., 558, A132, 2013.

Douglas, K. M., Blitz, M. A., Mangan, T. P., and Plane, J. M.: Experimental study of the removal of ground-and excited-state phosphorus atoms by atmospherically relevant species, The Journal of Physical Chemistry A, 123, 9469-9478, 2019.

505   Douglas, K. M., Blitz, M. A., Mangan, T. P., Western, C. M., and Plane, J. M.: Kinetic Study of the Reactions PO + O_2 and PO_2 + O_3 and Spectroscopy of the PO Radical, The Journal of Physical Chemistry A, 124, 7911-7926, 2020.

Drowart, J., Myers, C. E., Szwarc, R., Vander Auwera-Mahieu, A., and Uy, O. M.: Determination by the mass spectrometric Knudsen cell method of the atomization energies of the molecules PO and PO_2, Journal of the Chemical Society, Faraday Transactions 2: Molecular and Chemical Physics, 68, 1749-1757, 1972.

Dunning, T. H., Peterson, K. A., and Wilson, A. K.: Gaussian basis sets for use in correlated molecular calculations. X. The atoms aluminum through argon revisited, The Journal of chemical physics, 114, 9244-9253, 10.1063/1.1367373, 2001.

Eckert, F., Pulay, P., and Werner, H. J.: *Ab initio* geometry optimization for large molecules, J. Comput. Chem., 18, 1473-1483, 1997.

Francisco, J. S.: Coupled cluster study of the energetic and spectroscopic properties of OPO^x (x = O, + 1, −1), The Journal of chemical physics, 117, 3190-3195, 2002.

Gomes, A. C. R., Rocha, C. M. R., Jasper, A. W., and Galvão, B. R. L.: Formation of phosphorus monoxide through the $P(^4S) + O_2(^3\Sigma^-) \rightarrow O(^3P) + PO(^2\Pi)$ reaction, J. Mol. Model., 28, 259, 10.1007/s00894-022-05242-4, 2022.

Graff, M. M., and Wagner, A. F.: Theoretical studies of fine-structure effects and long-range forces: Potential-energy surfaces and reactivity of $O(^3P) + OH(^2\Pi)$, The Journal of chemical physics, 92, 2423-2439, 1990.

Hamilton, P. A.: The laser induced fluorescence spectrum and radiative lifetime of PO_2, The Journal of chemical physics, 86, 33-41, 1987.

Henshaw, T. L., MacDonald, M. A., Stedman, D. H., and Coombe, R. D.: The $P(^4S_u) + N_3$ ($^2\Pi_g$) reaction: chemical generation of a new metastable state of PN, Journal of Physical Chemistry, 91, 2838-2842, 1987.

Hernández, M. V., and Oro, J.: Primary sources of phosphorus and phosphates in chemical evolution, Origins of Life and Evolution of the Biosphere, 27, 459-480, 1997.

Huber, K.: Constants of diatomic molecules, Molecular spectra and molecular structure, 4, 146-291, 1979.

Husain, D., and Norris, P. E.: Reactions of phosphorus atoms, P ($3^4S_{3/2}$), studied by attenuation of atomic resonance radiation in the vacuum ultraviolet, Journal of the Chemical Society, Faraday Transactions 2: Molecular and Chemical Physics, 73, 1107-1115, 1977.

Husain, D., and Slater, N. K.: Time-resolved resonance fluorescence studies of ground state phosphorus atoms, P $[^3p^3(^4S_{3/2})]$, Journal of the Chemical Society, Faraday Transactions 2: Molecular and Chemical Physics, 74, 1627-1643, 1978.

Jarrett-Sprague, S. A., and Hillier, I. H.: *Ab initio* calculations of the structure and infrared spectrum of As_2O and As_4O, Chem. Phys., 148, 325-332, 1990.

Kabbadj, Y., and Liévin, J.: *Ab initio* study of the electronic structure of the PO_2 radical, Phys. Scr., 40, 259, 1989.

Kawaguchi, K., Saito, S., Hirota, E., and Ohashi, N.: Far-infrared laser magnetic resonance detection and microwave spectroscopy of the PO_2 radical, The Journal of chemical physics, 82, 4893-4902, 1985.

Knowles, P. J., and Werner, H.: An efficient second-order MC SCF method for long configuration expansions, Chem. Phys. Lett., 115, 259-267, 1985.

Knowles, P. J., and Werner, H.: An efficient method for the evaluation of coupling coefficients in configuration interaction calculations, Chem. Phys. Lett., 145, 514-522, 1988.

545   Lawson, M. A., Hoffman, K. J., and Davies, P. B.: Infrared diode laser spectroscopy of the v_3 fundamental band of the PO_2 free radical, J. Mol. Spectrosc., 269, 61-76, 2011.

Lefloch, B., Vastel, C., Viti, S., Jiménez-Serra, I., Codella, C., Podio, L., Ceccarelli, C., Mendoza, E., Lépine, J. R. D., and Bachiller, R.: Phosphorus-bearing molecules in solar-type star-forming regions: first PO detection, Mon. Not. Roy. Astron. Soc., 462, 3937-3944, 2016.

550   Lei, J., Teslja, A., Nizamov, B., and Dagdigian, P. J.: Free-jet electronic spectroscopy of the PO_2 radical, The Journal of Physical Chemistry A, 105, 7828-7833, 2001.

Li, J., Caridade, P. J., and Varandas, A. J.: Quasiclassical trajectory study of the atmospheric reaction $N(^2D) + NO(X\,^2\Pi) \rightarrow O(^1D) + N_2\,(X\,^1\Sigma_g^+)$, The Journal of Physical Chemistry A, 118, 1277-1286, 2014.

Li, X., Qin, Z., Li, J., and Liu, L.: An accurate NH_2 (X $^2A''$) CHIPR potential energy surface via extrapolation to
555   the complete basis set limit and dynamics of the N (^2D) + H_2 (X $^1\Sigma_g^+$) reaction, Phys. Chem. Chem. Phys., 24, 26564-26574, 2022.

Liang, J., Cui, F., Wang, R., Huang, W., and Cui, Z.: A general analytical expression for the three-dimensional Franck-Condon integral and simulation of the photodetachment spectrum of the PO_2^- anion, J. Mol. Spectrosc., 286, 12-20, 2013.

560   Liu, H., Shi, D., Sun, J., Zhu, Z., and Shulin, Z.: Accurate calculations on the 22 electronic states and 54 spin-orbit states of the O_2 molecule: Potential energy curves, spectroscopic parameters and spin-orbit coupling, Spectrochimica Acta Part A: Molecular and Biomolecular Spectroscopy, 124, 216-229, 2014.

Liu, H., Shi, D., Sun, J., and Zhu, Z.: Accurate potential energy curves and spectroscopic properties of the 27 Λ-S states and 73 Ω states of the PO radical, Mol. Phys., 115, 714-730, 2017.

565   Lodders, K.: Solar system abundances and condensation temperatures of the elements, The Astrophysical Journal, 591, 1220, 2003.

Lohr, L. L.: A theoretical study of the gaseous oxides PO_2 and PO, their anions, and their role in the combustion of phosphorus and phosphine, Journal of physical chemistry (1952), 88, 5569-5574, 1984.

Maciá, E.: The role of phosphorus in chemical evolution, Chem. Soc. Rev., 34, 691-701, 2005.

570   Martin, J. M. L., and Uzan, O.: Basis set convergence in second-row compounds. The importance of core polarization functions, Chem. Phys. Lett., 282, 16-24, 10.1016/S0009-2614(97)01128-7, 1998.

Murrell, J. N.: Molecular potential energy functions, edited, J. Wiley, 1984.

Pasek, M. A.: Rethinking early Earth phosphorus geochemistry, Proceedings of the National Academy of Sciences, 105, 853-858, 2008.

575   Peslherbe, G. H., Wang, H., and Hase, W. L.: Monte Carlo sampling for classical trajectory simulations, Advances in Chemical Physics, 105, 171-201, 1999.

Peverati, R., and Truhlar, D. G.: M11-L: A local density functional that provides improved accuracy for electronic

structure calculations in chemistry and physics, The Journal of Physical Chemistry Letters, 3, 117-124, 2012.

Plane, J. M., Flynn, G. J., Määttänen, A., Moores, J. E., Poppe, A. R., Carrillo-Sanchez, J. D., and Listowski, C.:
580   Impacts of cosmic dust on planetary atmospheres and surfaces, Space Sci. Rev., 214, 1-42, 2018.

Plane, J. M., Feng, W., and Douglas, K. M.: Phosphorus chemistry in the Earth's upper atmosphere, Journal of Geophysical Research: Space Physics, 126, e2021J-e29881J, 2021.

Prajapat, L., Jagoda, P., Lodi, L., Gorman, M. N., Yurchenko, S. N., and Tennyson, J.: ExoMol molecular line lists–XXIII. Spectra of PO and PS, Mon. Not. Roy. Astron. Soc., 472, 3648-3658, 2017.

585   Qian, H., Davies, P. B., and Hamilton, P. A.: High-resolution spectroscopic study of the oxidation of white phosphorus, Journal of the Chemical Society, Faraday Transactions, 91, 2993-2998, 1995.

Rivilla, V. M., Drozdovskaya, M. N., Altwegg, K., Caselli, P., Beltrán, M. T., Fontani, F., Van Der Tak, F., Cesaroni, R., Vasyunin, A., and Rubin, M.: ALMA and ROSINA detections of phosphorus-bearing molecules: the interstellar thread between star-forming regions and comets, Mon. Not. Roy. Astron. Soc., 492, 1180-1198, 2020.

590   Rocha, C., and Varandas, A.: Accurate CHIPR potential energy surface for the lowest triplet state of C_3, The Journal of Physical Chemistry A, 123, 8154-8169, 2019a.

Rocha, C., and Varandas, A.: A global CHIPR potential energy surface for ground-state C_3H and exploratory dynamics studies of reaction $C_2 + CH \rightarrow C_3 + H$, Phys. Chem. Chem. Phys., 21, 24406-24418, 2019b.

Rocha, C. M., and Varandas, A. J.: A general code for fitting global potential energy surfaces via CHIPR method:
595   Triatomic molecules, Comput. Phys. Commun., 247, 106913, 2020.

Rocha, C. M., and Varandas, A. J.: A general code for fitting global potential energy surfaces via CHIPR method: Direct-Fit Diatomic and tetratomic molecules, Comput. Phys. Commun., 258, 107556, 2021.

Rocha, C. M., Linnartz, H., and Varandas, A. J.: Reconciling spectroscopy with dynamics in global potential energy surfaces: The case of the astrophysically relevant SiC_2, The Journal of Chemical Physics, 157, 104301,
600   2022.

Schmidt, J. A., Johnson, M. S., Hattori, S., Yoshida, N., Nanbu, S., and Schinke, R.: OCS photolytic isotope effects from first principles: sulfur and carbon isotopes, temperature dependence and implications for the stratosphere, Atmos. Chem. Phys., 13, 1511-1520, 2013.

Sordo, J. A.: Performance of CCSDT for first row AB/AB$^-$ diatomics: Dissociation energies and electron affinities,
605   The Journal of Chemical Physics, 114, 1974-1980, 2001.

Tenenbaum, E. D., Woolf, N. J., and Ziurys, L. M.: Identification of phosphorus monoxide $(X\,^2\Pi_r)$ in VY Canis Majoris: Detection of the first po bond in space, The Astrophysical Journal, 666, L29, 2007.

Thomas, J. B., Waas, J. R., Harmata, M., and Singleton, D. A.: Control elements in dynamically determined selectivity on a bifurcating surface, J. Am. Chem. Soc., 130, 14544-14555, 2008.

610   Todd, Z. R.: Sources of Nitrogen-, Sulfur-, and Phosphorus-Containing Feedstocks for Prebiotic Chemistry in the Planetary Environment, Life, 12, 1268, 2022.

Varandas, A. N. J. C., and Murrell, J. N.: A many-body expansion of polyatomic potential energy surfaces:

application to H n systems, Faraday Discuss., 62, 92, 10.1039/dc9776200092, 1977.

Varandas, A.: A useful triangular plot of triatomic potential energy surfaces, Chem. Phys. Lett., 138, 455-461, 1987.

Varandas, A.: Combined-hyperbolic-inverse-power-representation of potential energy surfaces: A preliminary assessment for H_3 and HO_2, The Journal of Chemical Physics, 138, 54120, 2013.

Verma, R. D., and McCarthy, C. F.: A new spectrum of the PO_2 radical, Can. J. Phys., 61, 1149-1159, 1983.

Werner, H. J., and Knowles, P. J.: An efficient internally contracted multiconfiguration–reference configuration interaction method, The Journal of chemical physics, 89, 5803-5814, 1988.

Werner, H. J., Knowles, P. J., Knizia, G., Manby, F. R., Schütz, M., Celani, P., Györffy, W., Kats, D., Korona, T., and Lindh, R.: MOLPRO, version 2015.1, a package of ab initio programs, University of Cardiff Chemistry Consultants (UC3): Cardiff, Wales, UK, 2015.

Werner, H., Knowles, P. J., Manby, F. R., Black, J. A., Doll, K., Heßelmann, A., Kats, D., Köhn, A., Korona, T., and Kreplin, D. A.: The Molpro quantum chemistry package, The Journal of Chemical Physics, 152, 144107, 2020.

Woon, D. E., and Dunning Jr, T. H.: Gaussian basis sets for use in correlated molecular calculations. III. The atoms aluminum through argon, The Journal of chemical physics, 98, 1358-1371, 1993.

Xianyi, Z., Jun, W., Fei, W., and Zhifeng, C.: *Ab initio* calculations and Franck–Condon analysis of photoelectron spectra of PO_2, Journal of Molecular Structure: THEOCHEM, 851, 40-45, 2008.

Xu, C., de Beer, E., and Neumark, D. M.: Photoelectron spectroscopy of PO_2^-, The Journal of chemical physics, 104, 2749-2751, 1996.

Zeng, H., and Zhao, J.: Theoretical study of the structure and analytic potential energy function for the ground state of the PO_2 molecule, Chin. Phys. B, 21, 78202, 2012.

Zhang, D. H., and Zhang, J. Z.: Photofragmentation of HF dimer: Quantum dynamics studies on ab initio potential energy surfaces, The Journal of chemical physics, 99, 6624-6633, 1993.

Zhang, D. H., and Zhang, J. Z.: Quantum reactive scattering with a deep well: Time-dependent calculation for H + O_2 reaction and bound state characterization for HO_2, The Journal of chemical physics, 101, 3671-3678, 1994.

Zhao, Y., and Truhlar, D. G.: Exploring the limit of accuracy of the global hybrid meta density functional for main-group thermochemistry, kinetics, and noncovalent interactions, J. Chem. Theory Comput., 4, 1849-1868, 2008.

Ziurys, L. M., Schmidt, D. R., and Bernal, J. J.: New circumstellar sources of PO and PN: The increasing role of phosphorus chemistry in oxygen-rich stars, The Astrophysical Journal, 856, 169, 2018.